MATERIALS SCIENCE

Versatile synthesis of dendritic mesoporous rare earth–based nanoparticles

Hongyue Yu[1]†, Wenxing Wang[1]†, Minchao Liu[1], Tiancong Zhao[1], Runfeng Lin[1], Mengmeng Hou[1], Yufang Kou[1], Liang Chen[1], Ahmed A. Elzatahry[2], Fan Zhang[1], Dongyuan Zhao[1], Xiaomin Li[1]*

Rare earth–based nanomaterials that have abundant optical, magnetic, and catalytic characteristics have many applications. The controllable introduction of mesoporous channels can further enhance its performance, such as exposing more active sites of rare earth and improving the loading capacity, yet remains a challenge. Here, we report a universal viscosity-mediated assembly strategy and successfully endowed rare earth–based nanoparticles with central divergent dendritic mesopores. More than 40 kinds of dendritic mesoporous rare earth–based (DM-REX) nanoparticles with desired composition (single or multiple rare earth elements, high-entropy compounds, etc.), particle diameter (80 to 500 nanometers), pore size (3 to 20 nanometers), phase (amorphous hydroxides, crystalline oxides, and fluorides), and architecture were synthesized. Theoretically, a DM-REX nanoparticle library with 393,213 kinds of possible combinations can be constructed on the basis of this versatile method, which provides a very broad platform for the application of rare earth–based nanomaterials with rational designed functions and structures.

INTRODUCTION

As a type of important strategic resource, rare earth elements include 15 lanthanide elements (La-Lu) with unique electron configurations of [Xe] $4f^{n-1}5d^{0-1}6s^2$ (n = 1 to 15) and two other elements of scandium and yttrium (*1*). The unpaired 4f electrons of rare earth ions are typically not involved in chemical bonding, resulting in unique properties in terms of luminescence, electronic and magnetic properties, catalytic activities, etc. (*2*–*8*). In many applications (especially in catalysis), the performances always depend on the surface exposure of the rare earth ions (*9*, *10*). Benefiting from the merits of high surface area, low density, and abundant pore architectures, the introduction of mesopore channels with controllable architectures into the frameworks of rare earth–based nanoparticles provides an excellent choice for the further enrichment of their feature sets and applications (*11*–*16*).

In particular, dendritic mesoporous nanoparticles with tunable radial mesopore channels (3 to 20 nm) have been considered to be an ideal architecture for the diffusion, transport, and loading of the guest objects with different diameters, such as small molecules, macromolecules, and even nanoparticles (*17*–*22*). Great efforts have been devoted to synthesize mesoporous nanoparticles with unique dendritic architecture, and a few novel routes have been developed, such as growth kinetics control strategy, emulsion-induced interface assembly, oil-water biphase (or nanoemulsion) methods, etc. (*23*–*25*). However, the composition of the obtained dendritic mesoporous nanoparticles is limited to SiO_2, dopamine, resorcinol formaldehyde, Au, Pd, Pt, and Al_2O_3 (*26*–*32*). The mesostructure of the reported porous rare earth–based materials is disordered, and its structural parameters are difficult to be regulated (*33*, *34*). There are many challenges in the synthesis of rare earth–based nanoparticles with ordered and controllable mesostructure (*35*). First, the hydrolysis of rare earth precursors under alkaline conditions is very fast, and the hydrolyzed oligomers are easy to be aggregated to nonporous solid nanoparticles before they are co-assembled with the mesostructured-directing agent. Second, the controllable assembly and cross-linking among the oligomer/surfactants composite micelles are still very difficult. Last but not least, because the hydrolysis of various rare earth precursors are quite different, it is still a great challenge to generically synthesize the rare earth mesoporous nanoparticles with controllable composition, crystal phase, and architecture, especially for the high-entropy compounds with multiple rare earth elements.

Viscosity is one of the most important properties of a fluid. In chemical reactions, viscosity can affect the diffusion and aggregation kinetics of substances (e.g., the aforementioned hydrolyzed oligomers, surfactants, micelles, etc.). Inspired by this fact, here, we propose to regulate the micelles' diffusion and assembly kinetics by the viscosity (i.e., viscosity-mediated assembly strategy), which can be used to synthesize uniform dendritic mesoporous rare earth–based (DM-REX) nanoparticles, including the rare earth hydroxides [DM-RE$(OH)_x$], oxides (DM-REO_x), or fluorides (DM-Na_xREF_y). More than 40 kinds of DM-REX nanoparticles with single or multiple rare earth elements, high-entropy compounds, etc. are reported. The pore size of the obtained DM-REX with controllable particle size (80 to 500 nm) can be well tuned from 3 to 20 nm. This versatile viscosity-mediated assembly approach is also suitable for the construction of core@shell-structured nanocomposites regardless of the morphology, composition, and surface properties of the cores [Au nanorods, Prussian blue (PB) nanocubes, Fe_2O_3 nanospindles, SiO_2 nanospheres, and so on]. This study paves the way toward a reliable and versatile platform to achieve rational design and synthesis of DM-REX nanoparticles for various applications.

RESULTS

Controllable synthesis of dendritic mesoporous–gadolinium hydroxide

The DM-RE$(OH)_x$ nanoparticles could be prepared via a viscosity-mediated assembly strategy in the oil-water biphase system. Typically,

[1]Department of Chemistry, State Key Laboratory of Molecular Engineering of Polymers, iChem, Shanghai Key Laboratory of Molecular Catalysis and Innovative Materials, Fudan University, Shanghai 200433, China. [2]Materials Science and Technology Program, College of Arts and Sciences, Qatar University, P.O. Box 2713, Doha, Qatar.
*Corresponding author. Email: lixm@fudan.edu.cn
†These authors contributed equally to this work.

cyclohexane can be used as the oil phase, while the aqueous phase is a solution that contains hexadecyltrimethylammonium bromide (CTAB) as a structure-directing agent, hexamethylenetetramine (HMTA) as an alkali source, rare earth chlorides as precursors, and citric acid as chelating agent to regulate the hydrolysis of rare earth precursors and interaction between the hydrolyzed oligomers and CTAB. After the addition of "viscosity regulator" (sodium salicylate), the viscosity of water phase becomes very high (movie S1), which further influences the hydrolysis speed of rare earth precursors and the co-assembly of hydrolyzed oligomers and CTAB micelles, especially the diffusion and aggregation kinetics of oligomer/CTAB composite micelles (see the mechanism section). By regulating the viscosity, the uniform DM-REX nanoparticles with desired composition, particle diameter, pore size, crystal phase, and architecture were synthesized.

Taking the dendritic mesoporous–gadolinium hydroxide [DM-Gd(OH)$_x$] as a typical example, the scanning electron microscopy (SEM) and transmission electron microscopy (TEM) images show that the obtained DM-Gd(OH)$_x$ nanoparticles with a diameter of 200 nm are very uniform (Fig. 1, A to C, and fig. S1, A to C). The dendritic radial mesopore channels can be observed. The element mapping shows that gadolinium, oxygen, and carbon are evenly distributed in the nanoparticles (Fig. 1D). The nitrogen sorption isotherms of the DM-Gd(OH)$_x$ prepared by the viscosity-mediated assembly strategy exhibit typical type IV curves, and the Brunauer-Emmett-Teller (BET) surface area is measured to be as high as ~67 m^2/g. The pore size is estimated to be ~10.8 nm, which is consistent with the SEM and TEM observations (Fig. 1E). The small-angle x-ray scattering (SAXS) pattern shows a well-resolved scattering peak at q value of ~0.3 nm^{-1}, indicating that the mesopores of DM-Gd(OH)$_x$ have good uniformity (fig. S1D). Fourier transform infrared (FTIR) spectroscopy and thermogravimetric analysis (TGA) show abundant hydroxyl group in the sample, suggesting that the DM-Gd(OH)$_x$ is a rare earth hydroxide compound (fig. S2).

In addition, the pore size of DM-Gd(OH)$_x$ nanoparticles can be well tuned from 3 to 20 nm by increasing the oil/water volume ratio from 0 to 2:5 and further decreasing the concentration of $GdCl_3{\cdot}6H_2O$ from 1.5 to 0.5 mg/ml (Fig. 1F). With the increase in the pore size, the mesopore walls become thinner and thinner, and the BET surface area of the DM-Gd(OH)$_x$ nanoparticles also increases from 52 to 112 m^2/g (fig. S3). In addition, by simply adjusting the concentration of citric acid chelating agent from 0.1 to 0.4 mg/ml, the particle size of DM-Gd(OH)$_x$ can easily be adjusted from 80 to 500 nm (Fig. 1G).

The generality of the synthesis approach

As shown in Fig. 2A, almost all rare earth elements in the periodic table of elements can be fabricated into the DM-RE(OH)$_x$ nanoparticles with uniform spherical morphology, and opening dendritic mesopore channels can be controllably synthesized. It can be seen that the diameter and mesopore size of nanoparticles with different rare earth components are different (fig. S4), even under the same experimental conditions [e.g., the synthesis of DM-Ce(OH)$_x$,

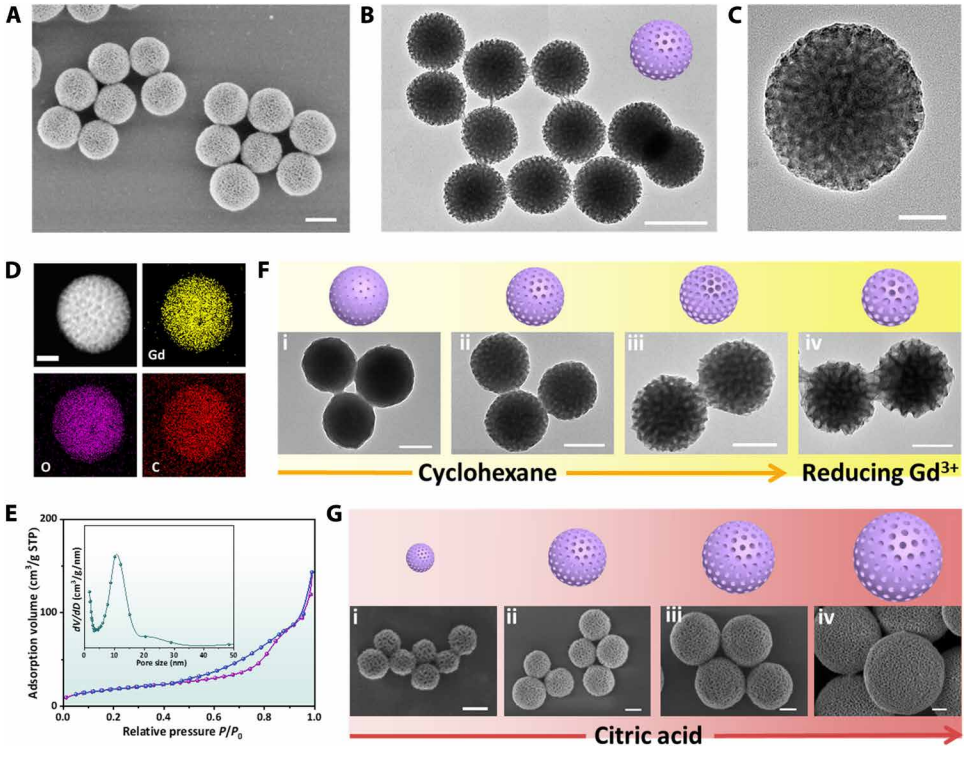

Fig. 1. Microstructure characterization of the DM-Gd(OH)$_x$ nanoparticles and controllability of the viscosity-mediated assembly strategy. (**A**) SEM, (**B** and **C**) TEM images with different magnifications, (**D**) element mappings, (**E**) nitrogen sorption isotherms, and pore size distribution of DM-Gd(OH)$_x$ (STP means standard temperature and pressure). (**F**) Scheme illustrations and TEM images of DM-Gd(OH)$_x$ nanoparticles with different pore sizes (3 to 20 nm) by tuning the amount of cyclohexane: (i) 0 ml, (ii) 2.0 ml, (iii) 4.0 ml, and (iv) 4.0 ml (the amount of $GdCl_3{\cdot}6H_2O$ were also decreased from 15 to 5 mg). (**G**) Scheme illustrations and SEM images of DM-Gd(OH)$_x$ nanoparticles with different particle sizes (80 to 500 nm) by simply tuning the concentration of citric acid: (i) 0.1 mg/ml, (ii) 0.2 mg/ml, (iii) 0.3 mg/ml, and (iv) 0.4 mg/ml. Scale bars, 50 nm (C and D), 100 nm (F and G), and 200 nm (A and B).

DM-Nd(OH)$_x$, and DM-Eu(OH)$_x$], mainly because the solubility product constant (K_{sp}) of each RE(OH)$_x$ is different. The K_{sp} of RE(OH)$_x$ products directly affects the nucleation and growth of RE(OH)$_x$ nanoparticles. The smaller the K_{sp} is, the easier it is to form hydroxide precipitation, which corresponds to the lower critical nucleation concentration, the increase in nuclei number, and the decrease in particle size. Anyway, for the nanoparticles containing specific rare earth elements, the variation rules of mesopore size and nanoparticle diameter are consistent with that of DM-Gd(OH)$_x$ mentioned above.

This viscosity-mediated assembly strategy is also suitable for the synthesis of DM-RE(OH)$_x$ nanoparticles with multiple rare earth elements. Regardless of the number of rare earth elements, the obtained multicomponent DM-RE(OH)$_x$ nanoparticles also have size uniformity and dendritic mesostructures with a high mesoporosity. The element mappings of the obtained DM-RE(OH)$_x$ nanoparticles from binary to denary show that rare earth elements are uniformly distributed in the framework of the mesoporous nanoparticles (Fig. 2, B to D, and fig. S5A). Energy-dispersive x-ray spectroscopy (EDS) and the corresponding quantitative analysis of the denary DM-RE(OH)$_x$ nanoparticles show that the proportion of each rare earth element is more than 5%, indicating that multicomponent DM-RE(OH)$_x$ nanoparticle is a kind of high-entropy material with dendritic mesopores (fig. S5B).

The transformation of DM-RE(OH)$_x$ into DM-REO$_x$ and DM-Na$_x$REF$_y$

The x-ray diffraction (XRD) pattern shows that the obtained DM-Gd(OH)$_x$ nanoparticles are amorphous (Fig. 3B). However, the DM-Gd(OH)$_x$ nanoparticles can be further transferred into crystalline dendritic mesoporous gadolinium oxide (DM-Gd_2O_3) nanoparticles after the calcination in the atmosphere of nitrogen and air at 600°C (Fig. 3, A to E, and fig. S6). The dendritic radial mesopore channels are retained very well in the DM-Gd_2O_3 nanoparticles, which are composed by many small α-phase Gd_2O_3 nanocrystals (~6 nm) (fig. S7, A to C). As one of the most important crystalline matrixes of the fluorescent nanomaterials, the cubic phase DM-$Na_5Gd_9F_{32}$ with unique dendritic radial mesostructure can also be synthesized from the DM-Gd_2O_3 nanoparticles after the hydrothermal treatment with NaF at 180°C (Fig. 3, A, B, and F to H, and fig. S7, D to F). Besides, these transformation strategies are also suitable for the synthesis of other rare earth element DM-REO$_x$ and DM-Na$_x$REF$_y$ nanoparticles (figs. S8, S10A, and S11, A and B).

Similar with the monocomponent DM-RE(OH)$_x$, the amorphous multicomponents DM-RE(OH)$_x$ nanoparticles can also be transferred into crystalline high-entropy DM-REO$_x$ and DM-Na$_x$REF$_y$ with multiple rare earth elements after the calcination or hydrothermal treatment (Fig. 4 and figs. S9; S10, B to D; and S11). The homogeneous distribution of rare earth ions makes the obtained

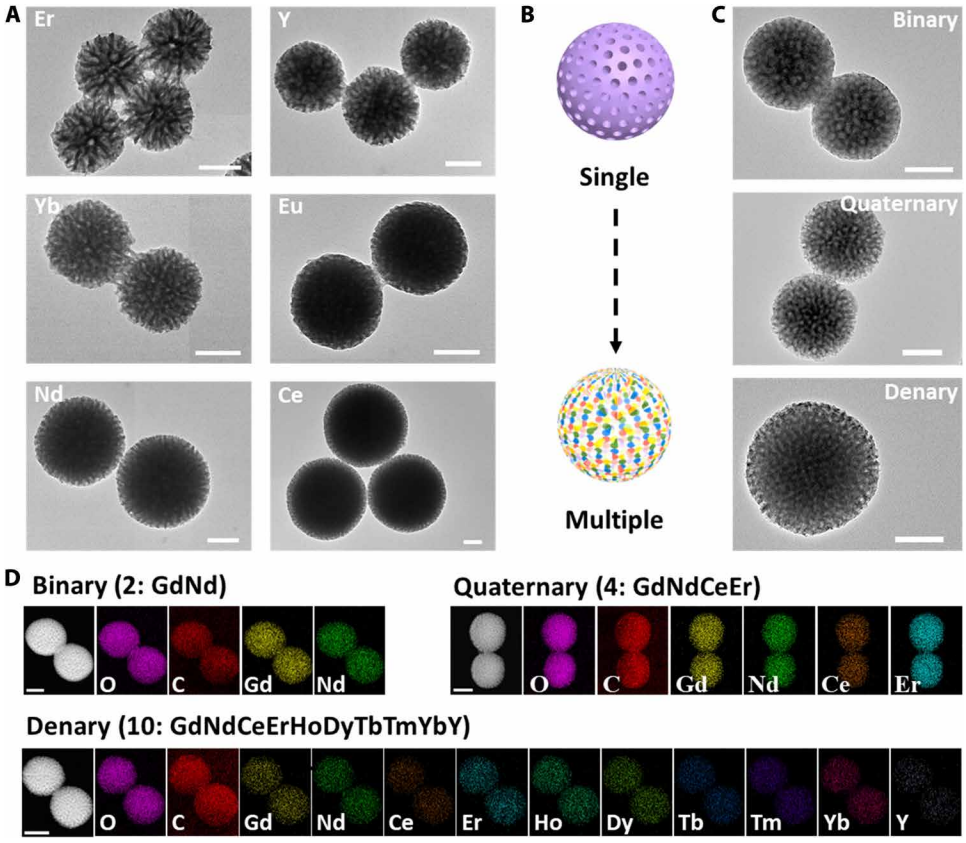

Fig. 2. The generality of the strategy for the synthesis of DM-RE(OH)$_x$ nanoparticles with controllable composites. (**A**) TEM images of the obtained DM-Er(OH)$_x$, DM-Y(OH)$_x$, DM-Yb(OH)$_x$, DM-Eu(OH)$_x$, DM-Nd(OH)$_x$, and DM-Ce(OH)$_x$, respectively. Scheme illustrations (**B**), TEM images (**C**), and element mappings (**D**) of DM-RE(OH)$_x$ with multiple rare earth elements. Scale bars, 100 nm.

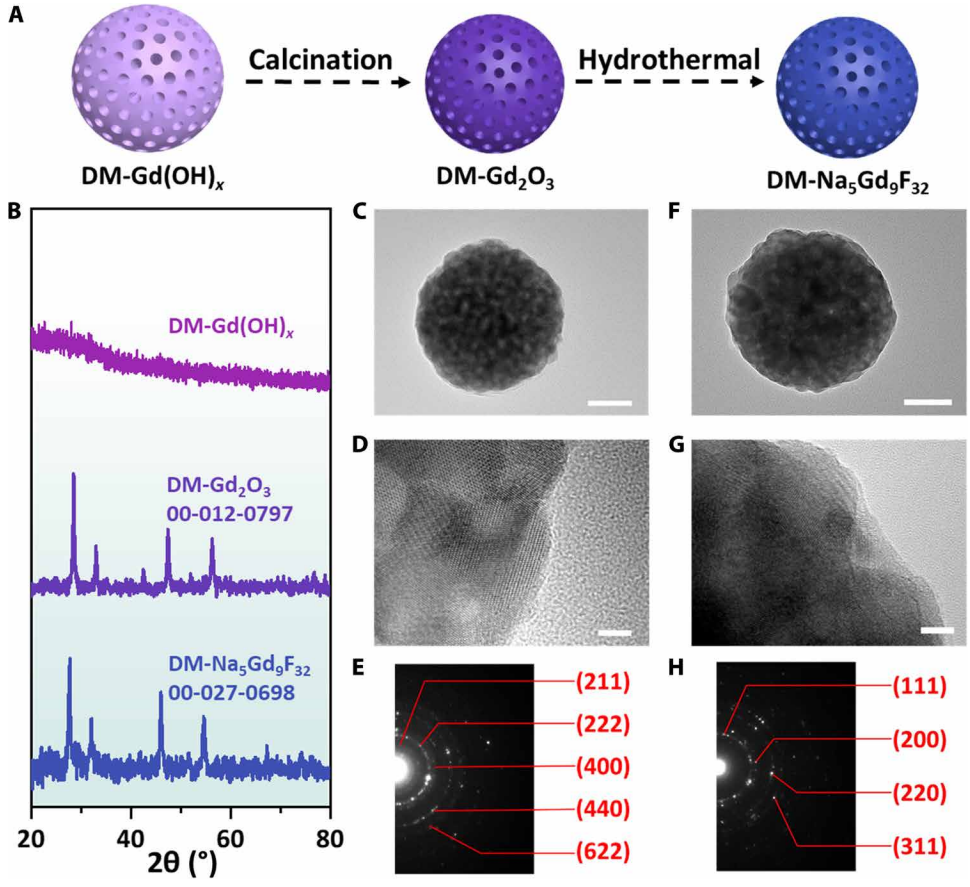

Fig. 3. Transformation of amorphous DM-Gd(OH)$_x$ nanoparticles into crystalline DM-Gd$_2$O$_3$ and DM-Na$_5$Gd$_9$F$_{32}$ nanoparticles. (**A**) Scheme illustrations and (**B**) XRD patterns of DM-Gd(OH)$_x$, DM-Gd$_2$O$_3$, and DM-Na$_5$Gd$_9$F$_{32}$ nanoparticles. TEM, high-resolution TEM images, and selected-area electron diffraction (SAED) patterns of (**C** to **E**) DM-Gd$_2$O$_3$ and (**F** to **H**) DM-Na$_5$Gd$_9$F$_{32}$. Scale bars, 50 nm (C and F) and 5 nm (D and G).

multicomponent DM-RE(OH)$_x$ nanoparticles particularly suitable for the synthesis of crystalline high-entropy compounds. The element mappings of one typical high-entropy nanoparticle show that all the expected rare earth ions are uniformly distributed in the framework of the mesoporous nanoparticles (Fig. 4, E and K), even in the high-entropy nanoparticle containing 10 kinds of rare earth elements. The XRD patterns show that, regardless of the number of rare earth elements, the crystal structure of the obtained high-entropy DM-REO$_x$ and DM-Na$_x$REF$_y$ nanoparticles is maintained without any phase separation (Fig. 4, D and J). Notably, the peaks shift slightly to lower angle in the high-entropy compounds, which can be attributed to the increase in the average diameter of rare earth ions, and a slightly expansion of unit cell. After the formation of high-entropy compounds, the grain size of the small nanocrystals in the DM-REX nanoparticles decreases, which further results in the broadening of the diffraction peaks.

So—including the hydroxides, oxides, and fluorides—there are 393,213 (131,071 × 3) kinds of possible combinations for the DM-REX (more than 40 typical examples have been verified in this work), which is a big DM-REX nanoparticle library for different applications.

Core@shell-structured DM-RE(OH)$_x$ nanocomposites

Besides high-entropy DM-REX nanoparticles with rare earth element homogeneous distribution, the core@shell-structured multicomponent DM-REX nanocomposites with unevenly distributed rare earth elements can also be rationally fabricated. As shown in Fig. 5A, the DM-Y(OH)$_x$ shell (with the pore size of 20 nm) can be uniformly coated on the presynthesized DM-Gd(OH)$_x$ nanoparticles (with the pore size of 10 nm) to form the uniform core@shell-structured DM-Gd(OH)$_x$@DM-Y(OH)$_x$ nanocomposites with the hierarchical dendritic mesopore channels (fig. S12). All the expected rare earth elements of Gd and Y can be detected and matched well with the relative positions in the core@shell-structured nanocomposites. Furthermore, the other non–rare earth functional entities can also be integrated with DM-REX by constructing the core@shell structure. Regardless of the composition, geometry, or surface properties of the core (Au nanorods, PB nanocubes, Fe_2O_3 nanospindles, and SiO_2 nanospheres), the DM-Gd(OH)$_x$ shell can be uniformly coated on the functional cores without aggregation (Fig. 5, B to E, and fig. S13). In addition, the pore size of the shells surrounding the core can also be well controlled (Fig. 5E).

The enhanced physicochemical properties of the obtained DM-REX

After the introduction of mesopore channels, the rare earth–based nanoparticles still show promising optical, magnetic, and catalytic properties (figs. S14, S17, and S19). The open mesopore channels can result in the increase in the contact interface between the DM-REX

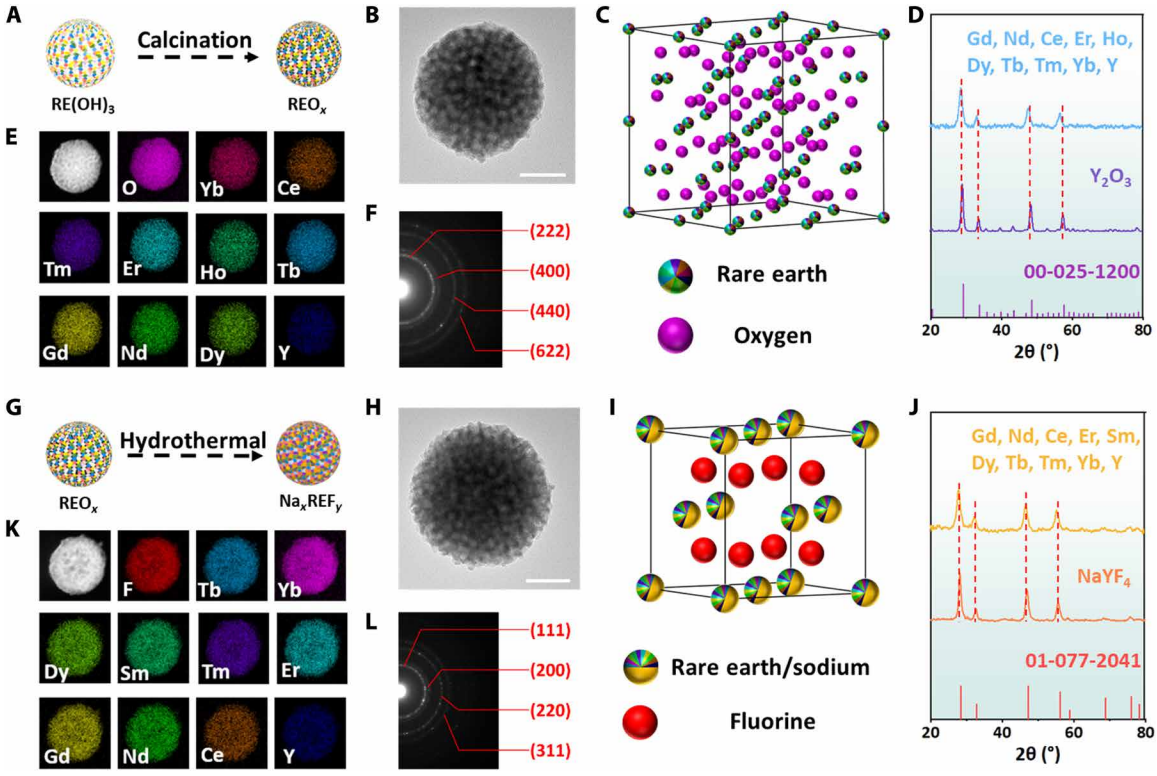

Fig. 4. The generality of the strategy for the synthesis of high-entropy DM-REO$_x$ and DM-Na$_x$REF$_y$ nanoparticles with controllable composites. Scheme illustrations, element mappings, TEM images, SAED, unit cells, and XRD patterns of DM-RE$_2$O$_3$ (including Ce, Nd, Gd, Tb, Dy, Ho, Er, Tm, Yb, and Y) (**A** to **F**) and DM-Na$_x$REF$_y$ (including Ce, Nd, Sm, Gd, Tb, Dy, Er, Tm, Yb, and Y) (**G** to **L**) with denary rare earth elements. Scale bars, 50 nm.

and external environment, leading to the extension and enhanced applications. As a proof of concept, the amorphous DM-Gd(OH)$_x$ and crystalline DM-CeO$_2$ were used as the models to investigate the biodegradability and catalytic activity of the obtained DM-REX compounds. In physiological environment of glutathione (GSH), the DM-Gd(OH)$_x$ nanoparticles can react with GSH to generate small molecular complex (*36*, *37*). Because of the presence of open dendritic mesopore channels, GSH in the solution can efficiently contact and react with amorphous Gd(OH)$_x$ framework. So, the degradation rate of the DM-Gd(OH)$_x$ nanoparticles with abundant mesopores is faster than that of the nonporous dense Gd(OH)$_x$ nanoparticles (figs. S15 and S16), which further results in the improved magnetic resonance imaging (MRI) of the tumor (fig. S17). CeO$_2$ is a typical peroxidase-mimicking catalyst. In catalysis, the maximum exposure of the active site is critical to the improvement of catalytic efficiency. So, because of the variation in surface area, there are substantial difference in the peroxidase-mimicking reaction kinetics under the catalysis of DM-CeO$_2$ with abundant mesopores (27 m^2/g) and dense CeO2 (13 m^2/g) nanoparticles (figs. S18 and S19). Compared to the dense CeO$_2$ (1.8×10^{-6} mM/s), the calculated maximum velocity (V_{max}) of DM-CeO$_2$ is increased by 370% (6.7×10^{-6} mM/s).

DISCUSSION

The mechanism of the viscosity-mediated assembly strategy

In this oil-water biphase system, the presence of sodium salicylate, which is used as a viscosity regulator, is the key to form the dendritic mesoporous nanoparticles. In the absence of sodium salicylate, the morphology of the obtained product changes from dendritic mesoporous nanospheres to irregular shapes (fig. S20). With the increase in sodium salicylate concentration from 0 to 1.2 mg/ml, the viscosity of the water phase initially remains unchanged (~1 mPa·s), then markedly increases to ~15 mPa·s, and eventually drops and stabilizes at ~8 mPa·s (fig. S21A). Three representative points (marked with blue stars: 1, 4, and 8 mPa·s) are selected to investigate the relationship between the viscosity of the solution and morphology of the product. It was found that the morphology of the products changed from irregular bulk material to dendritic mesoporous spheres with the increase in system viscosity (figs. S21, B to D, and S22).

On the basis of the above results, the viscosity-mediated assembly strategy is proposed for the synthesis of DM-REX nanoparticles. CTAB surfactants co-assemble with rare earth oligomers to form the composite micelles in the water phase with the assistant of citric acid (Fig. 6A) (*38*, *39*). The cyclohexane oil phase has two aspects of influence on the formation and assembly of the micelles. (i) It can swell the micelles by entering their hydrophobic cavity and, lastly, result in the increase in mesopore size. (ii) The oil-water interface provides two-dimensional interface for the heterogeneous aggregation of micelles to form the irregular bulk samples. Because of the lower energy consumption of the heterogeneous nucleation at the interface and the natural amphiphilic nature of surfactants, the critical nucleation concentration of heterogeneous aggregation of micelles at the oil-water interface (C_1) is lower than that of homogeneous assembly (C_2) in the aqueous phase (Fig. 6, D and E) (*40*, *41*).

The micelles' heterogeneous assembly at the oil-water interface (Fig. 6, D and E, green line) and homogeneous assembly in the

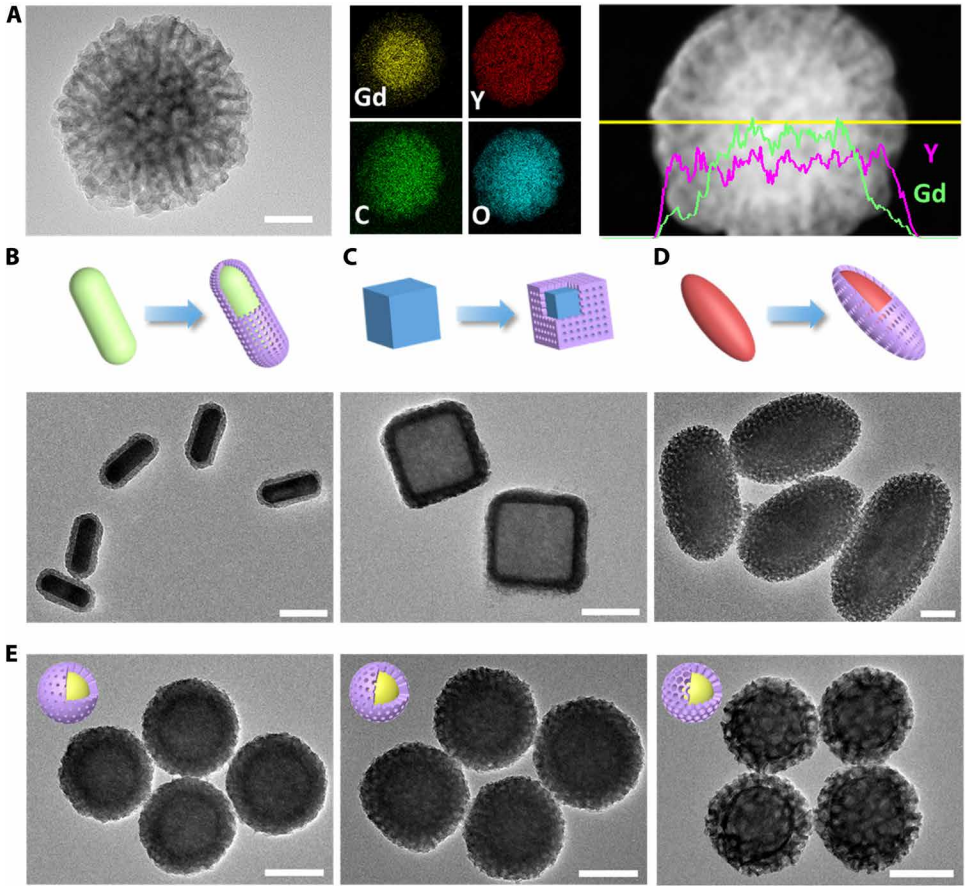

Fig. 5. The core@shell-structured DM-RE(OH)$_x$ nanocomposites. (**A**) TEM image, element mappings, and compositional line profiles of core@shell-structured DM-Gd(OH)$_x$@DM-Y(OH)$_x$. (**B** to **D**) Scheme illustrations and TEM images of DM-Gd(OH)$_x$ with different cores of Au nanorods, PB nanocubes, and spindle-shaped Fe_2O_3, respectively. (**E**) Scheme illustrations and TEM images of core@shell SiO_2@DM-Gd(OH)$_x$ with different pore sizes. Scale bars, 50 nm (A) and 100 nm (B to E).

aqueous solution (Fig. 6, D and E, red line) have a competitive relationship, which is closely related to the diffusion kinetic of the micelles from the aqueous phase to the oil-water interface. According to the theoretical simulation results, the diffusion kinetics of the micelles in the solution can be regulated by the tuning the viscosity of the solution (fig. S23). At a low viscosity (Fig. 6D), micelles in aqueous phase can rapidly diffuse to the oil-water interface and heterogeneously nucleate and cross-link at the interface to form irregular bulk samples (C_1, green line). In this case, the concentration of micelles in aqueous phase is difficult to accumulate and increase to the homogeneous critical nucleation concentration (C_2, red line). On the contrary, in the high-viscosity system (Fig. 6C), the diffusion of micelles to the oil-water interface is greatly suppressed, resulting in the rapid accumulation and increase in micelle concentration in the aqueous solution (red line), over homogeneous critical nucleation concentration (C_2), and we lastly realize the homogeneous assembly of the micelles to form dendritic mesoporous nanoparticles.

Besides the sodium salicylate, some other viscosity regulator (e.g., sodium benzoate and Gemini surfactant) can also be used for the synthesis of DM-RE(OH)$_x$ (fig. S24, A and B). In addition, the micelle assembly manner can be controlled by adjusting the temperature (equivalent to adjusting the viscosity of the solution), which further verifies the mechanism of viscosity-mediated micelles' homogenous assembly strategy (fig. S24, C and D).

The changes of other reactants in the system can affect the mesopore size and diameter of the obtained nanoparticles. With the increase in cyclohexane content (oil/water volume ratio), more cyclohexane can transfer into the hydrophobic core of micelles, which further results in the expansion of the mesopore. However, there is a limitation for the expansion effect of cyclohexane to CTAB micelles (the maximum is 15 nm). By reducing the content of $GdCl_3{\cdot}6H_2O$, the thickness of the mesopore wall can be reduced, which further results in the expansion of mesopore to 20 nm. The addition of more citric acid can enhance the acidity of the system, which is not conducive to the reaction, and the decrease in nucleation number of the system, further leading to the increase in particle size.

In summary, the viscosity-mediated assembly strategy is developed for the synthesis of dendritic mesoporous rare earth nanoparticles with monodispersed diameter. Theoretically, a DM-REX nanoparticle library with 393,213 kinds of possible combinations can be constructed on the basis of this versatile method (including hydroxides, oxides, and fluorides with single or multiple rare earth elements, high-entropy compounds, etc.). The pore size (3 to 20 nm) and particle diameter (80 to 500 nm) of the obtained dendritic mesoporous rare earth nanoparticles can be well controlled. Furthermore, this viscosity-mediated assembly approach also shows very broad applicability in the construction of rare earth–based core@shell-structured nanocomposites regardless of the morphology, composition,

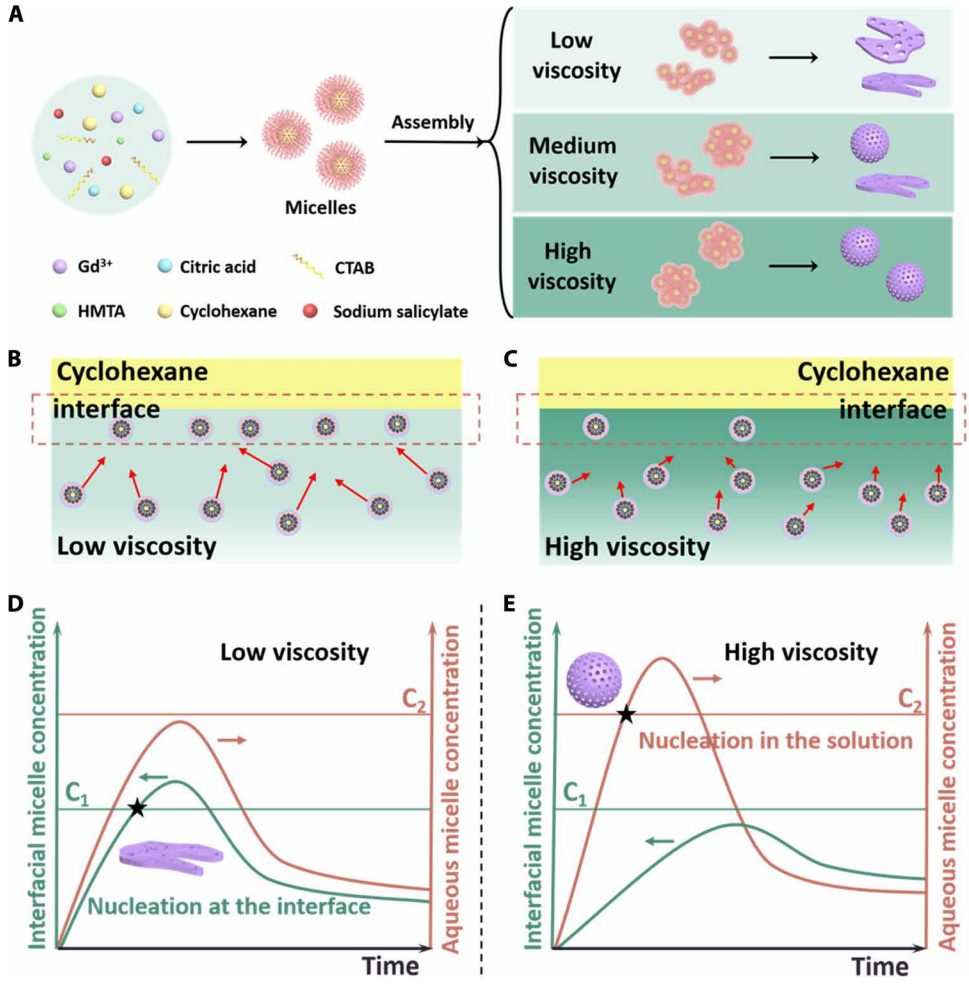

Fig. 6. The mechanism of the viscosity-mediated micelles' assembly strategy. (**A**) The scheme illustrations of the formation and assembly of the micelles in the different viscosity solutions. (**B** and **C**) The different diffusion behaviors of micelles in different viscosity systems. In low-viscosity system (left), the micelle diffusion rate is faster, so it is easier to diffuse from aqueous phase to the oil-water interface. In the high-viscosity system (right), the micelle diffusion is limited by high viscosity, and the micelle concentration at the oil-water interface is greatly different from that in the aqueous phase. (**D** and **E**) The scheme illustrations of the micelle concentration in the solution (homogeneous nucleation) and at the oil-water interface (heterogeneous nucleation) over time under different viscosity conditions. On the basis of LaMer model, in the solution with low viscosity (D), the heterogeneous nucleation of the micelles at the oil-water interface (green line) dominates the assembly of micelles to form the irregular bulk samples. In the solution with high viscosity (E), the homogeneous nucleation of the micelles in the aqueous phase (red line) dominates the assembly of micelles to form the dendritic mesoporous nanoparticles.

and surface properties of the cores. Last but not least, the mechanism of the viscosity-mediated assembly strategy is described. Introducing viscosity as a new variable into the synthetic system is expected to provide ideas for the synthesis of other inorganic materials. In addition to the promising optical, magnetic, catalytic properties of rare earth, the introduction of abundant mesopore channels can further enhance the applications of rare earth nanomaterials. We also expect that, with the unique dendritic mesoporous structure, the rare earth–based nanoparticles will show more excellent feature sets and applications in the future.

MATERIALS AND METHODS

Chemicals and reagents

CTAB (99%), octadecene (90%), polyvinyl pyrrolidone [PVP; weight-average molecular weight (M_w) = 44,000], and polyethyleneimine (PEI; M_w = 25,000) were purchased from Sigma-Aldrich. HMTA [chemically pure (CP)], citric acid [guaranteed reagent (AR)], ammonium hydroxide solution [28 weight % (wt %) NH_3 in H_2O], ethanol, iron(III) chloride hexahydrate ($FeCl_3{\cdot}H_2O$, 99%), ethylene glycol (AR), $AgNO_3$ (AR), sodium acetate (98%), HCl (37 wt %), chloroauric acid ($HAuCl_4$, AR), ascorbic acid (99.7%), thiourea (98%), and cyclohexane (AR) were purchased from Shanghai Chemical Reagents Co. Ltd. Gadolinium chloride hexahydrate ($GdCl_3{\cdot}6H_2O$, 99.9%), other rare earth chlorides, tetraethyl orthosilicate (TEOS; 99%), trisodium citrate, $K_3[Fe(CN)_6]{\cdot}3H_2O$ (99.95%), $NaBH_4$ (98%), sodium oleate (97%), sodium benzoate (99%), sodium fluoride (NaF; 99.99%), sodium citrate dihydrate (99.0%), and sodium salicylate (99.5%) were purchased from Aladdin Reagent Co. Ltd. Fetal bovine serum (FBS), penicillin-streptomycin, trypsin, and RPMI 1640 medium were provided by Gibco Life Technologies Co. All the chemicals and regents were used as received without any purification.

Synthesis of DM-RE(OH)$_x$ nanoparticles

The DM-RE(OH)$_x$ nanoparticles were synthesized via a viscosity-mediated micelle assembly strategy. Taking DM-Gd(OH)$_x$ as an example, 2.0 mg of citric acid, 20.0 mg of CTAB, 12.0 mg of sodium salicylate, 3.0 mg of HMTA, and 15.0 mg of $GdCl_3{\cdot}6H_2O$ were continuously added into 10.0 ml of water. After adding 2.0 ml of cyclohexane, the mixture was stirred vigorously for 1 hour. After reaction at 70°C for 7 hours, the product was separated by centrifugation and washed three times with ethanol. Last, the product was dispersed into 100 ml of ethanol, refluxed at 60°C for 4 hours, and repeated four times to remove the CTAB surfactant.

The pore size of the obtained DM-Gd(OH)$_x$ nanoparticles is about 10 nm, which can be adjusted by tuning the amount of cyclohexane and $GdCl_3{\cdot}6H_2O$. For example, the pore size is about 3 nm when 0 ml of cyclohexane and 15.0 mg of $GdCl_3{\cdot}6H_2O$ were used, the pore size is about 15 nm when 4.0 ml of cyclohexane and 15.0 mg of $GdCl_3{\cdot}6H_2O$ were used, and the pore size is about 20 nm when 4.0 ml of cyclohexane and 5.0 mg of $GdCl_3{\cdot}6H_2O$ were used.

The particle size can be adjusted by tuning the amount of citric acid. The diameter is about 80, 200, 350, and 500 nm when 1.0, 2.0, 3.0, and 4.0 mg of citric acid were used, respectively.

All the synthetic processes for other DM-RE(OH)$_x$ nanoparticles are the same, except for the rare earth chlorides precursors and the amount of citric acid. A total of 2.0 mg of citric acid was used to synthesize DM-Ce(OH)$_x$, DM-Nd(OH)$_x$, DM-Eu(OH)$_x$, and multiple rare earth elements DM-RE(OH)$_x$, and 4.0 mg of citric acid was used to synthesize DM-Er(OH)$_x$, DM-Yb(OH)$_x$, and DM-Y(OH)$_x$. The composites of the obtained DM-RE(OH)$_x$ nanoparticles with multiple rare earth elements were summarized in table S1.

Synthesis of DM-REO$_x$ nanoparticles

Taking the DM-Gd_2O_3 as an example, DM-Gd(OH)$_x$ nanoparticles were calcinated in a tubular furnace under N_2 with a ramp of 2°C/min to 600°C and held at 600°C for 6 hours. After that, the sample was further calcinated in air with a ramp of 3°C/min to 600°C for 2 hours to remove the residual carbon. All the calcination processes for different DM-REO$_x$ nanoparticles are the same, except that the calcination temperature of multiple-element DM-REO$_x$ is changed to 650°C in N_2. The composites of the obtained DM-REO$_x$ with multiple rare earth elements were summarized in table S2.

Synthesis of DM-Na$_x$REF$_y$ nanoparticles

Taking the DM-$Na_5Gd_9F_{32}$ nanoparticles as an example, 10.0 mg of DM-Gd_2O_3 and 15.0 mg of NaF were dissolved in 10.0 ml of deionized water. After stirring for 10 min, the mixture was transferred into a 25-ml Teflon-lined stainless steel autoclave, sealed, and heated at 180°C for 4 hours. The autoclave was allowed to cool down to room temperature naturally, and the products were separated by centrifugation and washed three times with deionized water. The composites of the obtained DM-Na$_x$REF$_y$ with multiple rare earth elements were summarized in table S3.

Synthesis of core@shell-structured DM-Gd(OH)$_x$@DM-Y(OH)$_x$ nanocomposites

The DM-Gd(OH)$_x$ core was prepared by adding 1.0 mg of citric acid, 20.0 mg of CTAB, 12.0 mg of sodium salicylate, 3.0 mg of HMTA, and 15.0 mg of $GdCl_3{\cdot}6H_2O$ into 10.0 ml of water. After adding 2.0 ml of cyclohexane, the mixture was stirred vigorously for 1 hour. After reaction at 70°C for 7 hours, the product was separated by centrifugation and washed three times with ethanol. The nanoparticles were dispersed into 10.0 ml of water.

Then, 2.0 mg of sodium citrate, 20.0 mg of CTAB, 12.0 mg of sodium salicylate, 3.0 mg of HMTA, 5.0 mg of $YCl_3{\cdot}6H_2O$, and 5.0 ml of cyclohexane were added into the obtained water solution of DM-Gd(OH)$_x$ (10.0 ml). The mixture was stirred vigorously for 1 hour. After reaction at 70°C for 7 hours, the product was separated by centrifugation and washed three times with ethanol.

Synthesis of core@shell-structured SiO_2@DM-Gd(OH)$_x$ nanocomposites with controllable pore size

SiO_2 nanoparticles with a diameter of 100 nm were prepared by a modified Stöber method (*42*). In general, 3.0 ml of TEOS was added to a solution containing 75.0 ml of ethanol, 10.0 ml of deionized water, and 1.0 ml of ammonia aqueous. After stirring and reaction for 5 hours, the products were collected by centrifugation and washed several times with ethanol and water. The obtained SiO_2 nanoparticles were, lastly, dispersed in 50 ml of water for further use.

Before the DM-RE(OH)$_x$ shell coating, the SiO_2 nanoparticles were surface-modified with PEI as follows. A total of 0.5 ml of SiO_2 nanoparticle solution was added to 1.5 ml of water containing 0.5 mg of PEI. After the ultrasonic dispersion for 20 min, the PEI-modified SiO_2 nanoparticles were centrifuged and washed three times with water. The nanoparticles were redispersed into 10.0 ml of water.

Then, 1.0 mg of citric acid, 20.0 mg of CTAB, 6.0 mg of sodium salicylate, 3.0 mg of HMTA, and 15.0 mg of $GdCl_3{\cdot}6H_2O$ were added into the obtained water solution of SiO_2-PEI nanoparticles (10.0 ml). The mixture was stirred vigorously for 1 hour. After reaction at 70°C for 7 hours, the product was separated by centrifugation and washed three times with ethanol. The pore size of the obtained DM-Gd(OH)$_x$ is about 3 nm, which can be adjusted by tuning the amount of cyclohexane. For example, the pore size is about 10 nm when 2.0 ml of cyclohexane was used, and the pore size is about 20 nm when 4.0 ml of cyclohexane was used.

Synthesis of core@shell-structured Au@DM-Gd(OH)$_x$ nanocomposites

Au nanorods were synthesized according to previous report (*43*). Typically, 10.0 ml of 0.5 mM $HAuCl_4$ was added into 10.0 ml of 0.2 M CTAB solution (marked with solution A). Then, 1.2 ml of 0.01 M $NaBH_4$ was diluted to 4.0 ml of water (marked with solution B). The B solution was added to the solution A under stirring to obtain the solution C. The color of the solution changed from yellow to brownish yellow. To prepare the growth solution, 3.5000 g of CTAB and 617.0 mg of sodium oleate were dissolved in 125.0 ml of water. Then, 9.0 ml of 4 mM $AgNO_3$ solution was added. The mixture was kept undisturbed at 30°C for 30 min. After that, 125.0 ml of 1 mM $HAuCl_4$ solution was added. The solution became colorless after 90 min, and 0.75 ml of HCl (37 wt %) was added. After 15 min, 0.625 ml of 0.064 M ascorbic acid was added and stirred for 1 min. Last, 0.2 ml of solution C was added. The mixture was stirred for 1 min and left undisturbed at 30°C for 24 hours. The final products were isolated by centrifugation and redispersed in 250 ml of water. The coating procedures are the same as those for the synthesis of SiO_2@DM-Gd(OH)$_x$, except that 10.0 ml of obtained Au nanorods was used as the cores, and the amount of other reactants are summarized in table S4.

Synthesis of core@shell-structured PB@DM-Gd(OH)$_x$ nanocomposites

PB nanoparticles were synthesized according to previous report (*44*). Typically, 3.0 g of PVP and 132.0 mg of $K_3[Fe(CN)_6]\cdot 3H_2O$ were added to 40.0 ml of HCl solution (0.01 M) under stirring. After magnetic stirring for 5 min, a clear solution was obtained. The solution was heated at 80°C for 20 hours. Then, the precipitates were collected by centrifugation and washed three times with ethanol. The PB nanoparticles were dispersed in 300 ml of water for further use. The coating procedures are the same as those for the synthesis of SiO_2@DM-Gd(OH)$_x$, except that 10.0 ml of obtained PB nanoparticles was used as the cores, and the amount of other reactants are summarized in table S4.

Synthesis of core@shell-structured Fe_2O_3@DM-Gd(OH)$_x$ nanocomposites

Spindle-shaped Fe_2O_3 nanoparticles were synthesized through a hydrothermal method reported previously (*45*). The Fe_2O_3 nanoparticles were prepared by aging 75.0 ml of solution of 0.02 M $FeCl_3$ and NaH_2PO_4 (0.2 mM) at 105°C for 50 hours. After cooling down to room temperature, the product was washed with distilled water and ethanol and, lastly, dispersed in 250 ml of water for further use. The coating procedures are the same as those for the synthesis of SiO_2@DM-Gd(OH)$_x$, except that the 10.0 ml of obtained spindle-shaped Fe_2O_3 nanoparticles was used as the cores, and the amount of other reactants is summarized in table S4.

Synthesis of DM-Gd(OH)$_x$ nanoparticles with sodium benzoate viscosity regulator

A total of 2.0 mg of citric acid, 5.0 mg of CTAB, 8.0 mg of sodium benzoate, 3.0 mg of HMTA, and 15.0 mg of $GdCl_3\cdot 6H_2O$ were continuously added into 10.0 ml of water. After adding 4.0 ml of cyclohexane, the mixture was stirred vigorously for 1 hour. After reaction at 70°C for 7 hours, the product was separated by centrifugation and washed three times with ethanol.

Synthesis of DM-Gd(OH)$_x$ nanoparticles with viscosity regulator of Gemini surfactant

Gemini surfactant ($C_{14\text{-}2\text{-}14}$) was synthesized according to previous report (*46*). A total of 30.0 mg of Gemini surfactant was dissolved in 10.0 ml of water at 60°C. After cooling to room temperature, 3.0 mg of citric acid, 3.0 mg of HMTA, and 15.0 mg of $GdCl_3\cdot 6H_2O$ were added in turn. After adding 4.0 ml of cyclohexane, the mixture was stirred vigorously for 1 hour. After reaction at 70°C for 7 hours, the product was separated by centrifugation and washed three times with ethanol.

Synthesis of dense Gd(OH)$_x$

Dense Gd(OH)$_x$ nanoparticles were synthesized by adding 2.0 mg of citric acid, 3.0 mg of HMTA, and 15.0 mg of $GdCl_3\cdot 6H_2O$ into 10.0 ml of water, and the mixture was stirred vigorously for 1 hour. After reaction at 70°C for 7 hours, the product was separated by centrifugation and washed three times with ethanol.

Simulation methods

The simulation is done using MATLAB. The length of the diffusion path is 1 mm. The solution of micelles (2 mg/ml) was placed at the middle of the diffusion path to diffuse freely. The diffusion obeys Fick's second law. Diffusion coefficient (D) was calculated from the experiment data, which the size of micelle is about 10 nm and the viscosity of solution is 1 and 8 mPa·s.

In vivo experiments

All the animal experiments were approved by the Shanghai Science and Technology Committee and performed in agreement with the guidelines of the Department of Laboratory Animal Science, Fudan University. For in vivo experiment, 4- to 6-week-old female Balb/c mice were commercially supplied by Slac Laboratory Animal Co. Ltd. (Shanghai, China). 4T1 cells were purchased from the cell bank of Chinese Academy of Science (Shanghai, China). The cells were cultured in standard RPMI 1640 medium supplemented with 10% (v/v) FBS, streptomycin (100 mg/ml), and penicillin (100 U/ml) at 37°C in a humidified incubator with 5% CO_2. 4T1 cells were detached from culture flask and suspended in FBS. Then, 4×10^6 cells were subcutaneously injected into the right back leg of mice. When the tumors grew large enough, 10 μl of DM-Gd(OH)$_x$ and dense Gd(OH)$_x$ (5.0 mg/ml) were intratumorally injected. The MRI was performed 24 hours later.

Characterization

TEM, high-resolution TEM, and the corresponding selected-area electron diffraction measurements were conducted on a JEM-2100F microscope (JEOL, Japan) operated at 200 kV coupled with EDS. SEM images were captured using field-emission SEM (FESEM; Hitachi S-4800, Japan). Samples used for TEM and FESEM analyses were prepared by dropping of the dispersions in ethanol on amorphous carbon-coated copper grids and silicon substrates, respectively. Wide-angle XRD data were recorded with a Bruker D8 powder x-ray diffractometer (Germany) using Cu K_α radiation (40 kV, 40 mA). SAXS measurements were taken on a NanoSTAR U SAXS system (Bruker, Germany) using Cu K_α radiation (40 kV, 35 mA). Nitrogen adsorption-desorption measurements were conducted to obtain information about the porosity. The measurements were conducted at 77 K with ASAP 2420 and Micromeritcs TriStar 3020 analyzer (USA). Before measurements, the samples were degassed in vacuum at 180°C for at least 12 hours. The BET method was used to calculate the specific surface areas, and the Barrett-Joyner-Halenda model was used to calculate the pore volumes and the pore size distributions derived from the adsorption branches of isotherms. TGAs were conducted on a Mettler Toledo TGA/SDTA851 analyzer from 25° to 800°C in N_2/air (20 ml/min) at a ramp rate of 10°C/min. The viscosity is measured by Usher viscometers. FTIR spectra were recorded using FTIR spectrometer (Thermo Fisher Scientific, Nicolet iS10, USA). The size distribution and zeta potential of the samples were recorded by using Zetasizer Nano ZS apparatus (Malvern, UK). MRI results were acquired by CG NOVILA 7.0 T (T_1-weighted images) from Shanghai Chenguang Medical Technologies Co. Ltd.

SUPPLEMENTARY MATERIALS

Supplementary material for this article is available at https://science.org/doi/10.1126/sciadv.abq2356

REFERENCES AND NOTES

1. T. Cheisson, E. J. Schelter, Rare earth elements: Mendeleev's bane, modern marvels. *Science* **363**, 489–493 (2019).
2. B. Ward-O'Brien, E. J. Pickering, R. Ahumada-Lazo, C. Smith, X. L. Zhong, Y. Aboura, F. Alam, D. J. Binks, T. L. Burnett, D. J. Lewis, Synthesis of high entropy lanthanide oxysulfides via the thermolysis of a molecular precursor cocktail. *J. Am. Chem. Soc.* **143**, 21560–21566 (2021).

3. P. Chen, W. Han, M. Zhao, J. Su, Z. Li, D. Li, L. Pi, X. Zhou, T. Zhai, Recent advances in 2D rare Earth materials. *Adv. Funct. Mater.* **31**, 2008790 (2020).
4. E. Skovran, N. Cecilia Martinez-Gomez, Just add lanthanides. *Science* **348**, 862–863 (2015).
5. G. Wang, G. Angelovski, Highly potent MRI contrast agent displaying outstanding sensitivity to zinc ions. *Angew. Chem. Int. Ed.* **60**, 5734–5738 (2021).
6. R. Ryoo, J. Kim, C. Jo, S. W. Han, J.-C. Kim, H. Park, J. Han, H. S. Shin, J. W. Shin, Rare-earth-platinum alloy nanoparticles in mesoporous zeolite for catalysis. *Nature* **585**, 221–224 (2020).
7. J. Liu, F. Li, Y. Wang, L. Pan, P. Lin, B. Zhang, Y. Zheng, Y. Xu, H. Liao, G. Ko, F. Fei, C. Xu, Y. du, K. Shin, D. Kim, S. S. Jang, H. J. Chung, H. Tian, Q. Wang, W. Guo, J.-M. Nam, Z. Chen, T. Hyeon, D. Ling, A sensitive and specific nanosensor for monitoring extracellular potassium levels in the brain. *Nat. Nanotechnol.* **15**, 321–330 (2020).
8. F. Wang, R. Deng, J. Wang, Q. Wang, Y. Han, H. Zhu, X. Chen, X. Liu, Tuning upconversion through energy migration in core-shell nanoparticles. *Nat. Mater.* **10**, 968–973 (2011).
9. S. Ji, Y. Qu, T. Wang, Y. Chen, G. Wang, X. Li, J. Dong, Q. Chen, W. Zhang, Z. Zhang, S. Liang, R. Yu, Y. Wang, D. Wang, Y. Li, Rare-Earth single erbium atoms for enhanced photocatalytic CO_2 reduction. *Angew. Chem. Int. Ed.* **59**, 10651–10657 (2020).
10. H. Wang, J. Qi, N. Yang, W. Cui, J. Wang, Q. Li, Q. Zhang, X. Yu, L. Gu, J. Li, R. Yu, K. Huang, S. Song, S. Feng, D. Wang, Dual-defects adjusted crystal-field splitting of $LaCo_{1-x}Ni_xO_{3-\delta}$ hollow multishelled structures for efficient oxygen evolution. *Angew. Chem. Int. Ed.* **59**, 19691–19695 (2020).
11. R. Mo, F. Li, X. Tan, P. Xu, R. Tao, G. Shen, X. Lu, F. Liu, L. Shen, B. Xu, Q. Xiao, X. Wang, C. Wang, J. Li, G. Wang, Y. Lu, High-quality mesoporous graphene particles as high-energy and fast-charging anodes for lithium-ion batteries. *Nat. Commun.* **10**, 1474 (2019).
12. P. Pei, Y. Chen, C. Sun, Y. Fan, Y. Yang, X. Liu, L. Lu, M. Zhao, H. Zhang, D. Zhao, X. Liu, F. Zhang, X-ray-activated persistent luminescence nanomaterials for NIR-II imaging. *Nat. Nanotechnol.* **16**, 1011–1018 (2021).
13. K. Shen, L. Zhang, X. Chen, L. Liu, D. Zhang, Y. Han, J. Chen, J. Long, R. Luque, Y. Li, B. Chen, Ordered macro-microporous metalorganic framework single crystals. *Science* **359**, 206–210 (2018).
14. L. Wang, M.-X. Chen, Q.-Q. Yan, S.-L. Xu, S.-Q. Chu, P. Chen, Y. Lin, H.-W. Liang, A sulfur-tethering synthesis strategy toward high-loading atomically dispersed noble metal catalysts. *Sci. Adv.* **5**, eaax6322 (2019).
15. L. Duan, C. Wang, W. Zhang, B. Ma, Y. Deng, W. Li, D. Zhao, Interfacial assembly and applications of functional mesoporous materials. *Chem. Rev.* **121**, 14349–14429 (2021).
16. T. Zhao, A. Elzatahry, X. Li, D. Zhao, Single-micelle-directed synthesis of mesoporous materials. *Nat. Rev. Mater.* **4**, 775–791 (2019).
17. J. Meng, Z. Jin, P. Zhao, B. Zhao, M. Fan, Q. He, A multistage assembly/disassembly strategy for tumor-targeted CO delivery. *Sci. Adv.* **6**, eaba1362 (2020).
18. X. Hong, X. Zhong, G. Du, Y. Hou, Y. Zhang, Z. Zhang, T. Gong, L. Zhang, X. Sun, The pore size of mesoporous silica nanoparticles regulates their antigen delivery efficiency. *Sci. Adv.* **6**, eaaz4462 (2020).
19. W. Chen, C. A. Glackin, M. A. Horwitz, J. I. Zink, Nanomachines and other caps on mesoporous silica nanoparticles for drug delivery. *Acc. Chem. Res.* **52**, 1531–1542 (2019).
20. C. Xu, C. Lei, Y. Wang, C. Yu, Dendritic mesoporous nanoparticles: Structure, synthesis and properties. *Angew. Chem. Int. Ed.* **61**, e202112752 (2022).
21. T. Zhao, X. Zhu, C.-T. Hung, P. Wang, A. Elzatahry, A. A. al-Khalaf, W. N. Hozzein, F. Zhang, X. Li, D. Zhao, Spatial isolation of carbon and silica in a single Janus mesoporous nanoparticle with tunable amphiphilicity. *J. Am. Chem. Soc.* **140**, 10009–10015 (2018).
22. B. Ding, S. Shao, C. Yu, B. Teng, M. Wang, Z. Cheng, K.-L. Wong, P. Ma, J. Lin, Large-pore mesoporous-silica-coated upconversion nanoparticles as multifunctional immunoadjuvants with ultrahigh photosensitizer and antigen loading efficiency for improved cancer photodynamic immunotherapy. *Adv. Mater.* **30**, e1802479 (2018).
23. W. Zhang, B. Li, Y. G. Sun, A. M. Cao, L. J. Wan, Spherical mesoporous metal oxides with tunable orientation enabled by growth kinetics control. *J. Am. Chem. Soc.* **142**, 17897–17902 (2020).
24. B. Y. Guan, L. Yu, X. W. D. Lou, Formation of asymmetric bowl-like mesoporous particles via emulsion-induced interface anisotropic assembly. *J. Am. Chem. Soc.* **138**, 11306–11311 (2016).
25. D. Shen, J. Yang, X. Li, L. Zhou, R. Zhang, W. Li, L. Chen, R. Wang, F. Zhang, D. Zhao, Biphase stratification approach to three-dimensional dendritic biodegradable mesoporous silica nanospheres. *Nano Lett.* **14**, 923–932 (2014).
26. Q. Tian, L. Jing, S. Ye, J. Liu, R. Chen, C.-A. H. Price, F. Fan, J. Liu, Nanospatial charge modulation of monodispersed polymeric microsphere photocatalysts for exceptional hydrogen peroxide production. *Small* **17**, e2103224 (2021).
27. M. Wu, Q. Meng, Y. Chen, Y. du, L. Zhang, Y. Li, L. Zhang, J. Shi, Large-pore ultrasmall mesoporous organosilica nanoparticles: Micelle/precursor co-templating assembly and nuclear-targeted gene delivery. *Adv. Mater.* **27**, 215–222 (2015).
28. J. Tang, A. K. Meka, S. Theivendran, Y. Wang, Y. Yang, H. Song, J. Fu, W. Ban, Z. Gu, C. Lei, S. Li, C. Yu, Openwork@dendritic mesoporous silica nanoparticles for lactate depletion and tumor microenvironment regulation. *Angew. Chem. Int. Ed.* **59**, 22054–22062 (2020).
29. B. Y. Guan, S. L. Zhang, X. W. D. Lou, Realization of walnut-shaped particles with macro–/mesoporous open channels through pore architecture manipulation and their use in electrocatalytic oxygen reduction. *Angew. Chem. Int. Ed.* **57**, 6176–6180 (2018).
30. H. Ataee-Esfahani, M. Imura, Y. Yamauchi, All-metal mesoporous nanocolloids: Solution-phase synthesis of core-shell Pd@Pt nanoparticles with a designed concave surface. *Angew. Chem. Int. Ed.* **52**, 13611–13615 (2013).
31. B. Jiang, C. Li, J. Tang, T. Takei, J. H. Kim, Y. Ide, J. Henzie, S. Tominaka, Y. Yamauchi, Tunable-sized polymeric micelles and their assembly for the preparation of large mesoporous platinum nanoparticles. *Angew. Chem. Int. Ed.* **55**, 10037–10041 (2016).
32. B. Jiang, C. Li, Ö. Dag, H. Abe, T. Takei, T. Imai, M. S. A. Hossain, M. T. Islam, K. Wood, J. Henzie, Y. Yamauchi, Mesoporous metallic rhodium nanoparticles. *Nat. Commun.* **8**, 15581 (2017).
33. C. Guo, X. Dong, X. Zhang, X. Cheng, Q. Li, Y. Sun, W. Liu, L. Huo, Y. Xu, Controllable construction of Ho_2O_3 nanomaterials with different dimensions (1D, 2D, and 3D) for real-time monitoring human breathing and body surface humidity detection. *J. Mater. Chem. A* **9**, 11632–11640 (2021).
34. H.-P. Zhou, Y.-W. Zhang, H.-X. Mai, X. Sun, Q. Liu, W.-G. Song, C.-H. Yan, Spontaneous organization of uniform CeO2 nanoflowers by 3D oriented attachment in hot surfactant solutions monitored with an in situ electrical conductance technique. *Chem. A Eur. J.* **14**, 3380–3390 (2008).
35. Y. Ren, Y. Zou, Y. Liu, X. Zhou, J. Ma, D. Zhao, G. Wei, Y. Ai, S. Xi, Y. Deng, Synthesis of orthogonally assembled 3D cross-stacked metal oxide semiconducting nanowires. *Nat. Mater.* **19**, 203–211 (2020).
36. B. Podányi, R. S. Reid, NMR study of the conformations of free and lanthanide-complexed glutathione in aqueous solution. *J. Am. Chem. Soc.* **110**, 3805–3810 (1988).
37. M. Zhao, R. Wang, B. Li, Y. Fan, Y. Wu, X. Zhu, F. Zhang, Precise in vivo inflammation imaging using in situ responsive cross-linking of glutathione-modified ultra-small NIR-II lanthanide nanoparticles. *Angew. Chem. Int. Ed.* **58**, 2050–2054 (2019).
38. Y. Ma, Y. Zhang, X. Wang, M. Fan, K. Li, T. Wang, Y. Liu, Q. Huo, Z.-A. Qiao, S. Dai, A chelation-induced cooperative self-assembly methodology for the synthesis of mesoporous metal hydroxide and oxide nanospheres. *Nanoscale* **10**, 5731–5737 (2018).
39. C. Wang, X. Wan, L. Duan, P. Zeng, L. Liu, D. Guo, Y. Xia, A. A. Elzatahry, Y. Xia, W. Li, D. Zhao, Molecular design strategy for ordered mesoporous stoichiometric metal oxide. *Angew. Chem. Int. Ed.* **58**, 15863–15868 (2019).
40. X. Li, L. Zhou, Y. Wei, A. M. el-Toni, F. Zhang, D. Zhao, Anisotropic growth-induced synthesis of dual-compartment Janus mesoporous silica nanoparticles for bimodal triggered drugs delivery. *J. Am. Chem. Soc.* **136**, 15086–15092 (2014).
41. Y. Wang, J. He, C. Liu, W. H. Chong, H. Chen, Thermodynamics versus kinetics in nanosynthesis. *Angew. Chem. Int. Ed.* **54**, 2022–2051 (2015).
42. W. Stöber, A. Fink, Controlled growth of monodisperse silica spheres in the micron size range. *J. Colloid Interface Sci.* **26**, 62–69 (1968).
43. W. Wang, P. Wang, X. Tang, A. A. Elzatahry, S. Wang, D. al-Dahyan, M. Zhao, C. Yao, C.-T. Hung, X. Zhu, T. Zhao, X. Li, F. Zhang, D. Zhao, Facile synthesis of uniform virus-like mesoporous silica nanoparticles for enhanced cellular internalization. *ACS Cent. Sci.* **3**, 839–846 (2017).
44. M. Hu, S. Furukawa, R. Ohtani, H. Sukegawa, Y. Nemoto, J. Reboul, S. Kitagawa, Y. Yamauchi, Synthesis of Prussian blue nanoparticles with a hollow interior by controlled chemical etching. *Angew. Chem. Int. Ed.* **51**, 984–988 (2012).
45. X. W. Lou, L. A. Archer, A general route to nonspherical anatase TiO_2 hollow colloids and magnetic multifunctional particles. *Adv. Mater.* **20**, 1853–1858 (2008).
46. F. M. Menger, J. S. Keiper, Gemini Surfactants. *Angew. Chem. Int. Ed.* **39**, 1906–1920 (2000).
47. Y. Yin, R. M. Rioux, C. K. Erdonmez, S. Hughes, G. A. Somorjai, A. P. Alivisatos, Formation of hollow nanocrystals through the nanoscale Kirkendall effect. *Science* **304**, 711–714 (2004).
48. S. Gao, H. Lin, H. Zhang, H. Yao, Y. Chen, J. Shi, Nanocatalytic tumor therapy by biomimetic dual inorganic nanozyme-catalyzed cascade reaction. *Adv. Sci.* **6**, 1801733 (2019).
49. H. Yan, Z. Han, K. Li, G. Li, X. Wei, Molecular dynamics simulation of the pH-induced structural transitions in CTAB/NaSal solution. *Langmuir* **34**, 351–358 (2018).

Acknowledgments: We appreciate S. Tao and J. He from Shanghai Chenguang Medical Technologies Co. Ltd. for the MRI measurement. The animal experiments were approved by the Shanghai Science and Technology Committee and were carried out according to the guidelines of Fudan University's administrative panel on laboratory animal care. **Funding:** This work was supported by the National Natural Science Foundation of China (22075049, 21875043, 22088101, 21701027, 21733003, 21905052, and 51961145403), National Key R&D Program of China (2018YFA0209401 and 2017YFA0207303), Key Basic Research Program of

Science and Technology Commission of Shanghai Municipality (17JC1400100), Natural Science Foundation of Shanghai (18ZR1404600, 20490710600, and 22ZR1478900), Shanghai Rising-Star Program (20QA1401200), and Qatar National Research Fund (a member of the Qatar Foundation) (NPRP grant no. NPRP 12S-0309-190268). **Author contributions:** Conceptualization: H.Y., W.W., and X.L. Synthesis: H.Y. and W.W. Investigation: H.Y., W.W., M.L., M.H., and L.C. Analysis: H.Y., W.W., M.L., T.Z., R.L., M.H., Y.K., and L.C. Simulation: R.L. and Y.K. Funding acquisition: F.Z., A.A.E., D.Z., and X.L. Supervision: X.L. Writing—original draft: H.Y., W.W., and M.L. Writing—review and editing: H.Y., W.W., F.Z., A.A.E., D.Z., and X.L. **Competing interests:** The authors declare that they have no competing interests. **Data and materials availability:** All data needed to evaluate the conclusions in the paper are present in the paper and/or the Supplementary Materials.

Submitted 27 March 2022
Accepted 15 June 2022
Published 29 July 2022
10.1126/sciadv.abq2356